ACS APPLIED ENGINEERING MATERIALS

Coupling Joule Heating with Vibration Ball Milling for Synthesizing Carbon-Supported $Ni_{100-x}Fe_x$ Nanoparticles Achieving Efficient Oxygen Evolution and Alkaline Water Electrolysis

Li Zhang,[§] Mengyuan Ma,[§] Zhenya Hu, Hui Liu, Dong Chen, Shaonan Tian,* Lin Xu,* Guozhu Chen,* and Jun Yang*

Cite This: https://doi.org/10.1021/acsaenm.4c00591 Read Online

ACCESS | Metrics & More | Article Recommendations | Supporting Information

ABSTRACT: Rapid and cost-effective synthesis of electrocatalysts for oxygen evolution reaction (OER) poses a significant technical challenge for the commercialization of water electrolysis. We, herein, report a facile strategy that couples quick Joule heating with mechanical ball milling for synthesizing well-defined $Ni_{100-x}Fe_x$ ($0 \leq x \leq 100$) alloy nanoparticles on carbon substrate toward high-efficiency OER and water splitting. This synthetic strategy involves first simply mixing the precursors and carbon substrate through ball milling and subsequent Joule heating on an electrical device for fast forming carbon-supported alloy nanoparticles with fine sizes and uniform distribution. In particular, the single-component Ni/C nanoparticles (i.e., $x = 0$) synthesized by this way include both fcc and hcp crystal phases, with the highest proportion of hcp phase at 370 °C, which endows the Ni/C nanoparticles with better OER activity than that of Ni/C samples synthesized at other temperatures. In addition, the $Ni_{100-x}Fe_x/C$ nanoparticles at an appropriate Ni/Fe ratio of 72/28 ($Ni_{72}Fe_{28}/C$) exhibit the best OER electrocatalysis, with a low overpotential of only 276 mV at a current density of 10 mA cm^{-2}, due to the optimal electronic interaction between Ni and Fe in the alloys. More importantly, under simulated industrial electrolysis conditions (30 wt % KOH at 60 °C), a two-electrode alkaline electrolyzer assembled with $Ni_{72}Fe_{28}/C$ at the anode and commercial Pt/C at the cathode ($Ni_{72}Fe_{28}/C||Pt/C$) requires only 1.39 V to deliver the current density of 100 mA cm^{-2}, along with an excellent 120-h durability at the same current density.

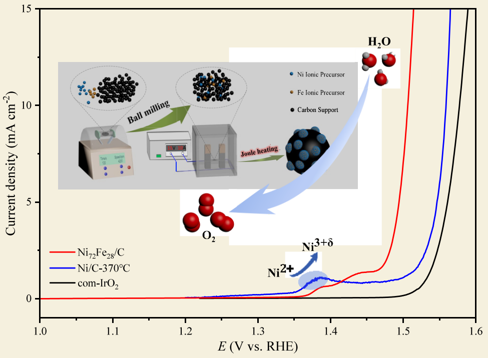

KEYWORDS: *Electrocatalyst, Oxygen evolution reaction, Water electrolysis, Joule heating, Ball milling*

INTRODUCTION

Hydrogen (H_2), a clean, carbon-free product with high energy density, holds great promise for replacing fossil fuels.[1,2] Water electrolysis is a commercially valuable and promising method for the large-scale production of high-purity H_2. Unfortunately, the key half-reaction of water electrolysis, i.e., oxygen evolution reaction (OER) that involves four proton-coupled electron transfer steps,[3] results in inherently sluggish kinetics and necessitates high overpotentials to proceed.[4,5] To date, noble metal oxides such as IrO_2 and RuO_2 have been regarded as the best OER electrocatalysts in terms of activity and durability. However, their high cost and scarcity severely hinder their commercialization in the water electrolysis toward industrial H_2 production.[6,7]

In recent years, nickel (Ni)-based electrocatalysts, including Ni nanoparticles,[8,9] NiOOH,[10−12] layered double hydroxides,[13−15] and phosphides,[16−18] have been extensively studied as excellent alternatives to noble metal-based catalysts for water electrolysis due to their abundant raw material sources and high electrocatalytic activity.[19−22] Among them, Ni nanoparticles stand out for their simple preparation process and low cost, making them highly marketable as OER catalysts in alkaline electrolytes. By modifying the surface structure and composition through the strategies like carbon support hybridization,[23,24] metal doping,[25−27] and phase control,[28,29] the initial OER activity of Ni nanoparticles could be improved to the level of existing industrial OER catalysts. Particularly, due to synergistic electronic interactions, alloys formed by Ni and other transition metals exhibit better OER activity than pure Ni.[18] For example, the diverse chemical states of iron (Fe) endow the NiFe bimetallic alloys at an appropriate Ni/Fe ratio with enhanced OER activity.[30−32] Additionally, different crystalline phases that have various metal atom stackings usually have different electronic properties, which would also greatly affect the intrinsic catalytic performance of metal

Received: September 18, 2024
Revised: November 7, 2024
Accepted: November 15, 2024

nanoparticles.[33,34] For instance, the hexagonal close-packed (hcp) bimetallic NiFe nanoparticles exhibit better OER activity than that of face-centered cubic (fcc) phase with consistent morphology and similar carbon shell structures.[35] Notably, recent studies have also highlighted the importance of high-valence Ni species ($Ni^{3+\delta}$) as active sites in enhancing OER activity.[36−38]

Furthermore, the synthesis of OER electrocatalysts is often time-consuming and complex, posing a significant technical challenge for the rapid development and commercialization of water electrolysis. Traditional preparation methods, such as solvothermal synthesis[39] and electrochemical deposition,[40] require multiple operational steps and long reaction times, making them costly and inconvenient for practical applications. Additionally, organic solvents and other impurities used during synthesis typically remain adsorbed on the catalyst surface and are difficult to fully remove, inevitably hindering the contact between active sites and the electrolyte, thus suppressing the overall electrochemical performance. Recently, Joule heating devices have been widely applied in catalyst preparations due to their highly sensitive temperature control and capability to generate ultrahigh temperatures.[41,42] The Joule heating method enables the simple, low-cost, and efficient synthesis of uniformly sized and well-dispersed nanoparticles.[43,44] Ball milling is a mechanical technique that rapidly, cleanly, and efficiently grinds and homogenizes precursors.[45,46] Unlike the synthetic strategies that prepare precursors in the liquid phase, ball milling only requires mixing and milling precise quantities of reagents, thereby avoiding the attachment of impurities from the liquid phase to the precursors, which could affect catalyst preparation and performance. To the best of our knowledge, the combination of ball milling with Joule heating for catalyst preparation has yet to be applied for overall water splitting.

In this context, this study proposes a simple and rapid ball milling-Joule heating method for synthesizing carbon-supported $Ni_{100-x}Fe_x$ nanoparticles at different temperatures, which are denoted as $Ni_{100-x}Fe_x$/C-T, where the T means temperature and $0 \leq x \leq 100$. In this strategy, we use an efficient vibrating ball mill to grind the mixture of carbon substrate and metal precursors with different Ni/Fe feeding ratios, and then reduce them on an electrical device that is capable to generate Joule heat. We noticed that for single-component Ni/C nanoparticles (i.e., $x = 0$), in addition to common fcc structure, their crystal phase also contains a certain proportion of hcp structure, and the latter reaches its maximum at an appropriate temperature (370 °C), which also endows the Ni/C-370 °C nanoparticles with better OER activity than that of Ni/C synthesized at other temperatures. Further, owing to the electronic interaction between Ni and Fe, the $Ni_{100-x}Fe_x$/C nanoparticles at a Ni/Fe ratio of 72/28 and 370 °C ($Ni_{72}Fe_{28}$/C-370 °C) exhibit the best electrocatalysis for OER, with a low overpotential of 276 mV at a current density of 10 mA cm^{-2}. In particular, under simulated industrial electrolysis conditions (30 wt % KOH at 60 °C), a two-electrode alkaline electrolyzer assembled with $Ni_{72}Fe_{28}$/C-370 °C at anode and commercial Pt/C at cathode ($Ni_{72}Fe_{28}$/C-370 °C||com-Pt/C) requires only a voltage of 1.39 V to deliver the current density of 10 mA cm^{-2}, along with a excellent 120-h durability at the current density of 100 mA cm^{-2}. This study therefore provides a fast and economical approach for producing high-efficiency electrocatalysts for practical anion exchange membrane water electrolysis (AEMWE).

EXPERIMENTAL SECTION

Reagents and Materials

Nickel acetylacetonate ($Ni(acac)_2$, 95%), iron acetylacetonate ($Fe(acac)_2$, 98%), and potassium hydroxide (KOH, 90%) from Shanghai Macklin Biochemical Co., Ltd., Nafion solution (5% in a mixture of low-fat alcohol and water) from DuPont, ethanol (>99.7%) from Beijing Chemical Works, carbon paper from Shanghai Hesen Company, Vulcan XC-72 carbon black (XC-72C, particle size of 40−50 nm) from Cabot Corporation, IrO_2 from Alfa Aesar, commercial Pt/C (20% Pt) from Johnson Matthey, Fumasep FAS-PET-75, a nonreinforced anion exchange membrane (AEM), from Fumatech (Germany) were used as received. An ultrasonic precision sprayer, model UC320, from Siansonic was used to spray the catalyst onto the carbon paper. The anion exchange membrane water electrolyzer (AEMWE) setup was assembled by using an electrolysis cell DA102 from Sinero. Ultrapure water was used throughout the study.

Preparation of $Ni_{100-x}Fe_x$/C-T Precursors

To synthesize the $Ni_{100-x}Fe_x$/C-T precursors with a mass loading of 20%, the theoretical mass ratio of $Ni_{100-x}Fe_x$ to the carbon substrate was set at 1:4. The masses of Ni and Fe were calculated based on their theoretical atomic ratios, which were set at 1:0, 10:1, 2:1, 1:1, 1:2, 1:10, and 0:1. Below are preparation details for a typical $Ni_{100-x}Fe_x$/C-T precursor: For the preparation of Ni_2Fe/C-T precursors, 135.3 mg of $Ni(acac)_2$, 90.1 mg of $Fe(acac)_2$, and 173.3 mg of XC-72C were added to a ball milling jar along with 1.6 mL of zirconia microbeads. The jar was then sealed with a lid. The ball milling jar was placed in a high-speed vibrating ball mill, secured with clamps, and the milling parameters were set to a rotational speed of 4200 rpm for 120 s. The entire precursor preparation process involves 10 ball milling cycles. After each cycle, the jar was cooled to prevent overheating, which could affect the precursor and the milling jar. The high-speed impacts of the zirconia microbeads in the ball milling jar cause the precursor to agglomerate, affecting the milling efficiency. Therefore, after every two milling cycles, the mixture was removed, ground in a mortar to break up the aggregates, and then returned to the ball milling jar for continued milling. After ten cycles of ball milling, the Ni_2Fe/C-T precursor was obtained. The preparation steps for other $Ni_{100-x}Fe_x$/C-T precursors were the same as those described above.

Synthesis of $Ni_{100-x}Fe_x$/C-T Nanoparticles

A 3 × 5 cm^2 piece of carbon cloth is clamped between two carbon rods, with 50.0 mg of $Ni_{100-x}Fe_x$/C-T precursor placed on it. The assembly is then placed into a custom vacuum chamber with the two carbon rods connected to electrode wires. The vacuum chamber door is closed to ensure a proper seal. Air is evacuated from the chamber using a vacuum pump to achieve a pressure of −14 atm. Subsequently, a 5% H_2 and 95% Ar gas mixture is introduced continuously into the chamber until it is filled with the gas mixture. During the entire heating process, the 5% H_2 and 95% Ar gas mixture is introduced at a flow rate of 20 mL min^{-1}.The heating temperature is controlled by adjusting the current with a Joule heating device. The initial current is set to 1.00 A, increased by 0.40 A every 5 min until the temperature reaches 200 °C. During the gradual heating process, $Ni(acac)_2$ and $Fe(acac)_2$ decompose to form NiO_n and FeO_n. The current is then further adjusted to raise the temperature to T (T = 220 °C, 270 °C, 320 °C, 370 °C, or 420 °C), and heating is continued for 30 min. During this stage, the oxides are reduced by H_2 to form $Ni_{100-x}Fe_x$ alloys, resulting in $Ni_{100-x}Fe_x$/C-T catalysts.

Characterizations

Transmission electron microscopy (TEM) and high-resolution TEM (HRTEM) imaging were performed by using a JEOL JEM-2010F electron microscope. The element distributions in the as-prepared samples were analyzed using an energy-dispersive X-ray spectroscopy (EDX) analyzer attached to TEM in scanning transmission electron microscopy (STEM) mode. High-angle annular dark-field scanning TEM (HAADF-STEM) imaging was conducted on an aberration-corrected JEM-ARM 200F at 300 kV, with a nominal image resolution of 0.07 nm, and the element distribution was analyzed by using an EDX analyzer. Powder X-ray diffraction (XRD) patterns were recorded on a Rigaku SmartLab (9KW) using Cu Kα radiation (λ = 0.154056 nm). X-ray photoelectron spectroscopy (XPS) was conducted on an AXIS SUPRA+ spectrometer to characterize the chemical states of relevant elements. Inductively coupled plasma atomic emission spectrometry (ICP-AES) measurements were performed on an Agilent 5800VDV instrument to analyze the elemental composition. In situ (electrochemical) Raman spectra were obtained by using a confocal Raman spectrometer with a 532 nm laser (Horiba LabRAM HR Evolution, Japan). Electrochemical tests were carried out using potentiostats (Biologic VMP3 and PRINCETON PARSTAT 4000A).

Electrochemical Measurements

The catalyst inks were prepared as follows: 5 mg of catalyst was ultrasonically dispersed in 1 mL of a solution consisting of 800 μL of anhydrous ethanol, 680 μL of ultrapure water, and 20 μL of Nafion solution to form a suspension. Then, 37.5 μL of the ink was taken and dropped onto a glassy carbon electrode, followed by drying using an infrared lamp.

Electrochemical measurements were conducted in a standard three-electrode cell connected to a potentiostat. The working electrode was an L-shaped glassy carbon electrode (d = 8 mm); the counter electrode was a Pt mesh (1 × 1 cm^2) attached to a Pt wire, and the reference electrode was a leak-free Ag/AgCl electrode. All potential values in the electrochemical measurements were calibrated against the reversible hydrogen electrode (RHE) using the equation $E_{\mathrm{RHE}} = E_{\mathrm{Ag/AgCl}} + 0.059 \times \mathrm{pH} + 0.197$. The overpotential ($\eta$) was calculated using the equation $\eta = E_{\mathrm{RHE}} - 1.23$ V. High-purity N_2 was bubbled through the electrolyte of 1.0 M KOH to purify it. The catalyst was fully activated by cyclic voltammetry (CV) with different scan rates of 200, 100, and 50 mV s^{-1} over the potential range of 0.824−2.024 V vs RHE. After purging the electrolyte with high-purity O_2 for 30 min to ensure saturation, the polarization curves were measured in O_2-saturated 1.0 M KOH using linear sweep voltammetry (LSV) at a scan rate of 5 mV s^{-1} over the potential range of 0.824−1.724 V vs RHE. The LSV curves from the three-electrode cell tests were corrected using 100% *iR* compensation. The current density was normalized by the electrode area (0.503 cm^2)) and the corresponding catalyst mass loading to obtain the specific activity and mass-based activity of the catalysts. The electrochemical active surface area (ECSA) was evaluated using the double-layer capacitance (C_{dl}), which was measured by cyclic voltammetry (CV) at different scan rates (50, 100, 150, 200, and 250 mV s^{-1}) within the non-Faradaic potential window (0.524−0.624 V vs RHE).The C_{dl} value was calculated from the slope of the plot of the average current density (j_{avg}) versus the scan rate (v), where $j_{\mathrm{avg}} = (j_{\mathrm{pos}} + |j_{\mathrm{neg}}|)/2$ at 1.074 V vs RHE, using the equation $j_{\mathrm{avg}} = C_{\mathrm{dl}} \cdot V$. Electrochemical impedance spectroscopy (EIS) measurements were conducted at 1.624 V vs RHE with a sinus amplitude of 5 mV over a frequency range of 200−0.01 Hz. The stability of the catalysts was assessed at an overpotential corresponding to a current density of 10 mA cm^{-2}.

Overall Water Splitting Measurements

Overall water splitting was conducted using a two-electrode configuration with carbon paper as both the anode and cathode supports. The as-prepared $Ni_{100-x}Fe_x$/C-T and commercial IrO_2 (com-IrO_2) powder loaded on the XC-72 carbon substrate were used as the anode catalysts, while the commercial Pt/C catalyst was used as the cathode catalyst. Catalyst inks were prepared by ultrasonically mixing 10 mL of anhydrous ethanol, 7.5 mL of ultrapure water, 420 μL of Nafion solution, and the corresponding catalyst powders. All catalysts have a loading of 2.0 mg cm^{-2}. The catalyst inks were uniformly applied onto 1 × 1 cm^2 carbon paper using an ultrasonic precision sprayer at a flow rate of 2.0 mL min^{-1}. The LSV curves of the overall water splitting device were recorded in 1.0 M KOH at a scan rate of 5 mV s^{-1} (without *iR* compensation). The stability of the overall water splitting was evaluated using chronoamperometry at an overpotential corresponding to a current density of 10 mA cm^{-2}. Additionally, water electrolysis was driven by a commercial AA battery with a nominal voltage of 1.5 V.

AEMWEs Measurements

Using carbon paper as the gas diffusion layer for both the cathode and the anode, $Ni_{100-x}Fe_x$/C-T or com-IrO_2 was sprayed onto the carbon paper as the anode catalyst layer, and commercial Pt/C was used as the cathode catalyst layer. Fumasep FAS-PET-75 was employed as the anion exchange membrane, and AEMWEs were assembled using metal bipolar plates (gold-plated). The preparation method for the catalyst-loaded carbon paper was the same as in the two-electrode configuration, with a spraying rate of 4.0 mL min^{-1}. The carbon paper has an area of 4 × 4 cm^2, with the anode catalyst layer loading of 1.3 mg cm^{-2} and the cathode catalyst layer loading of 2.0 mg cm^{-2}. The area resistance of the membrane electrode assembly (MEA) was evaluated in the cell using a two-electrode electrochemical impedance spectroscopy (EIS) method. The sinus amplitude and frequency range of the EIS locator were set to 10 mV and 1−0.1 Hz, respectively. The MEA, with an active area of 4 cm^2, was immersed in an electrolyte (30 wt % KOH) at 25 °C for area resistance measurements. A heating rod and thermocouple were inserted into the AEMWEs ports and connected to a temperature controller for constant temperature heating.

RESULTS AND DISCUSSION

Syntheses and Characterizations of Single-Component Ni/C-T

As shown by Figure 1A for the synthetic scheme, we first mix the Ni and Fe precursors as well as carbon substrate using vibration ball milling and then subject the mixture to Joule heating on an electrical device for forming $Ni_{100-x}Fe_x$ alloy particles on the carbon substrate. Our synthesis starts with the preparation of single-component Ni/C particles at different temperatures (Ni/C-T), i.e., x = 0. The crystal structure of the Ni/C-T nanoparticles was examined by X-ray diffraction (XRD). As disclosed by Figure 1B, a number of unique features could be noticed for the single-component Ni/C samples: (1) At low temperature, e.g. 220 °C, the Ni precursors cannot be reduced on carbon substrate, and hence, no characteristic diffraction peaks corresponding to Ni metal could be identified; (2) impressively, with the increase of temperature, on the XRD patterns of Ni/C-T samples, in addition to the diffraction peaks corresponding to the conventional fcc structure, i.e. the peaks located at 2θ of 44.5°, 51.8°, and 76.4° that match well with the (111), (200), and (220) planes of fcc Ni metal (JCPDS 04−0850), diffraction peaks corresponding to the hcp phase also appear, e.g. the peaks at 2θ of 39.1°, 41.5°, 44.5°, 58.4°, 71.0°, and 78.0°, which correspond to the (010), (002), (011), (012), (110), and (103) planes of hcp Ni (JCPDS 45−1027), suggesting that the carbon-supported Ni nanoparticles synthesized by coupling Joule heating with ball milling strategy possess a mixed structure of cubic and hexagonal phases; (3) initially, as the synthetic temperature increases, the characteristic peaks corresponding to hcp-Ni phase become more visible, e.g. the Ni/C samples from 270 to 370 °C, but the diffraction intensity of these characteristic peaks decreases at higher temperature, e.g. Ni/C-420 °C. By deconvoluting the peaks at 2θ of ca. 44.5 °C that contain both (111) signal of fcc-Ni and (011) signal of hcp-Ni, we can determine the percentages of hcp phase in different Ni/C-T samples, which are 42.19%, 47.50%, 54.50%, and 16.56% for Ni/C-270 °C, Ni/C-320 °C, Ni/C-370 °C, and Ni/C-420 °C, respectively, as seen in Figure S1 of Supporting Information (SI). The results indicate that the proportion of hcp-Ni in the Ni/C

https://doi.org/10.1021/acsaenm.4c00591
ACS Appl. Eng. Mater. XXXX, XXX, XXX−XXX

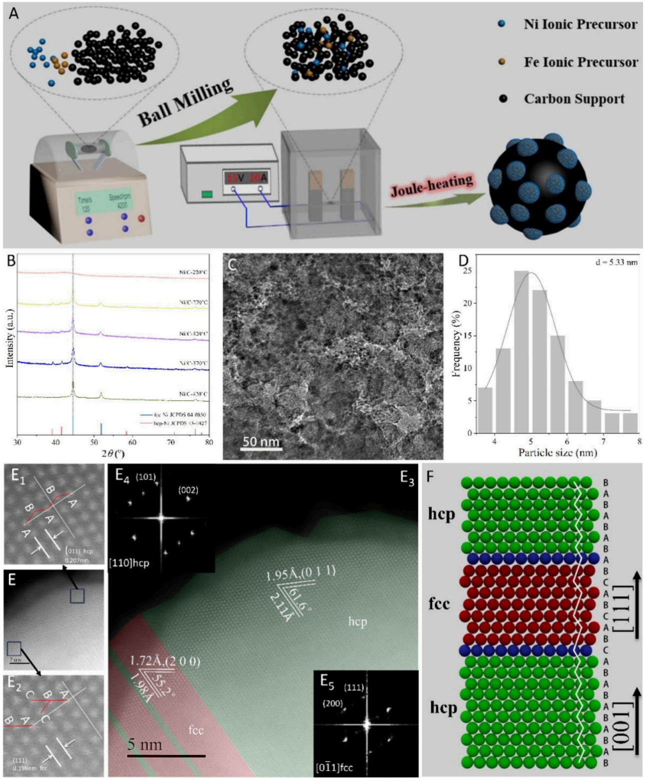

Figure 1. (A) Schematic illustration showing the synthesis of $Ni_{100-x}Fe_x$/C-T nanoparticles by coupling Joule heating with ball milling strategy; (B) XRD patterns of single-component Ni/C-T nanoparticles (from top to bottom: T = 220 °C, 270 °C, 320 °C, 370 and 420 °C); (C) TEM image and (D) histogram showing particle size distribution of the Ni/C-370 °C nanoparticles; (E) aberration-corrected HAADF-STEM image of a typical Ni nanoparticle of the Ni/C-370 °C sample; (E_1−E_3) magnified HAADF-STEM images of (E) showing the fcc and hcp domains, and (E_4,E_5) corresponding fast Fourier transform patterns; (F) atomic scale schematics showing the stacking sequence of hcp/fcc phase and domain boundary.

nanoparticles first gradually increases with the increase of synthetic temperature, reaching its highest value at 370 °C, and then decreases with further increase of the temperature.

Although both of them are close-packed structures, the three-dimensional fcc and hcp crystals are not identical as the stacking arrangement of Ni atomic planes are different, i.e., stacking sequence of ABCABC—for the former, while ABAB—for the latter.[47] In general, the Ni atoms tend to adopt a fcc arrangement mode; however, the rapid temperature increase caused by Joule heating and the hydrogen reduction atmosphere may lead to alterations in the kinetic parameters of crystal growth such as changes in growth rate, driving force, atomic diffusion coefficient, and deviations from the equilibrium state of the system, all of which could potentially contribute to the emergence of the hcp-Ni phase. At even higher temperatures, the intensified thermal vibrations make the atoms within the lattice become more unstable, and the hcp-Ni gradually transforms again into the more stable fcc-Ni as the latter is less prone to structural relaxation. This can explain the experimental observations that hcp-Ni first increases and then decreases in the Ni/C-T samples as the temperature rises.

Figure 1C and D show the TEM image and particle size histogram of the carbon-supported Ni nanoparticle synthesized at 370 °C (i.e., Ni/C-370 °C) using the ball milling-Joule heating method, which illustrate the Ni nanoparticles with an average size of 5.33 nm uniformly distribute on the carbon substrate. The HAADF-STEM image (Figure 1E) clearly shows that the Ni particles in the Ni/C-370 °C sample possess high crystallinity, in which the hcp-Ni and fcc-Ni domains could be clearly observed through a partial amplification technique (Figure 1E_1 and E_2, respectively). The amplified HAADF-STEM image, i.e., Figure 1E_3, reveals that the hcp and fcc domains in a Ni nanoparticle are separated by a boundary line. Particularly, in the hcp-Ni domain that has a corresponding fast Fourier transform (FFT) pattern with a [110] zone axis (Figure 1E_4), two crystal planes with different orientations and an interplanar angle of 61.6° have interplanar spacings of 2.07 and 1.95 Å, respectively. In contrast, in the fcc-Ni domain having a corresponding FFT pattern with a $[0\bar{1}1]$ zone axis (Figure 1E_5), the interplanar spacings of the two nonparallel crystal planes with an interplanar angle of 55.2° between them are1.98 and 1.72 Å, respectively. Figure S2 for the magnified HAADF-STEM image of a Ni nanoparticle with different phase domains and Figure 1F for a schematic diagram vividly demonstrates the detailed atomic stacking arrangements along the [111] direction in the fcc phase and along the [001] direction in the hcp phase, respectively.

The TEM images as well as their corresponding particle size histograms for the carbon-supported Ni nanoparticles synthesized at other temperatures (i.e., 220 °C, 270 °C, 320 °C, and 420 °C) are shown in Figure S3. As seen, under all temperatures, the particles have uniform dispersion on the carbon substrate, and the average sizes for Ni nanoparticles in Ni/C-220 °C, Ni/C-270 °C, Ni/C-320 °C, and Ni/C-420 °C are 1.49, 1.91, 3.56, and 8.82 nm, respectively. The gradually increasing particle size with the increase of synthetic temperatures indicates that despite the presence of carbon substrate, the Ni nanoparticles still undergo rapid ripening at high temperatures.

Electrocatalytic Evaluation of the Ni/C-T for OER

Before preparing the carbon-supported $Ni_{100-x}Fe_x$ alloy nanoparticles, we first tested the OER electrocatalytic activity of the Ni/C-T samples, so as to determine the optimal temperature for producing the NiFe alloys. The OER electrocatalysis of Ni/C-T nanoparticles and commercial IrO_2 catalyst (com-IrO_2) were measured in 1.0 M KOH electrolyte using a typical three-electrode system. In general, the overpotential for delivering a current density of 10 mA cm^{-2} (η_{10}) and mass-based activities is adopted to indicate the activities of the electrocatalysts. The actual Ni mass loading on carbon substrate for all Ni/C-T was determined using ICP-AES and is listed in Table S1.

As shown by Figure 2A and B for the linear sweep voltammetry (LSV) curves of Ni/C-T and com-IrO_2, which are normalized by the geometrical area of electrode and total metal mass loaded on the electrode, respectively, the Ni/C-370 °C sample has the best OER activity with an overpotential of 302 mV at η_{10} and mass-based activity of 80.3 mA mg^{-1}, respectively, which are better than those of carbon-supported Ni nanoparticles synthesized at other temperatures and com-IrO_2 catalyst. Further, as observed from the histograms showing the comparison of overpotentials for Ni/C-T and com-IrO_2 at current density of 10 mA cm^{-2} and mass activities at 1.53 V vs RHE, the overpotential first decreases with increasing synthetic temperature until 370 °C and then begins

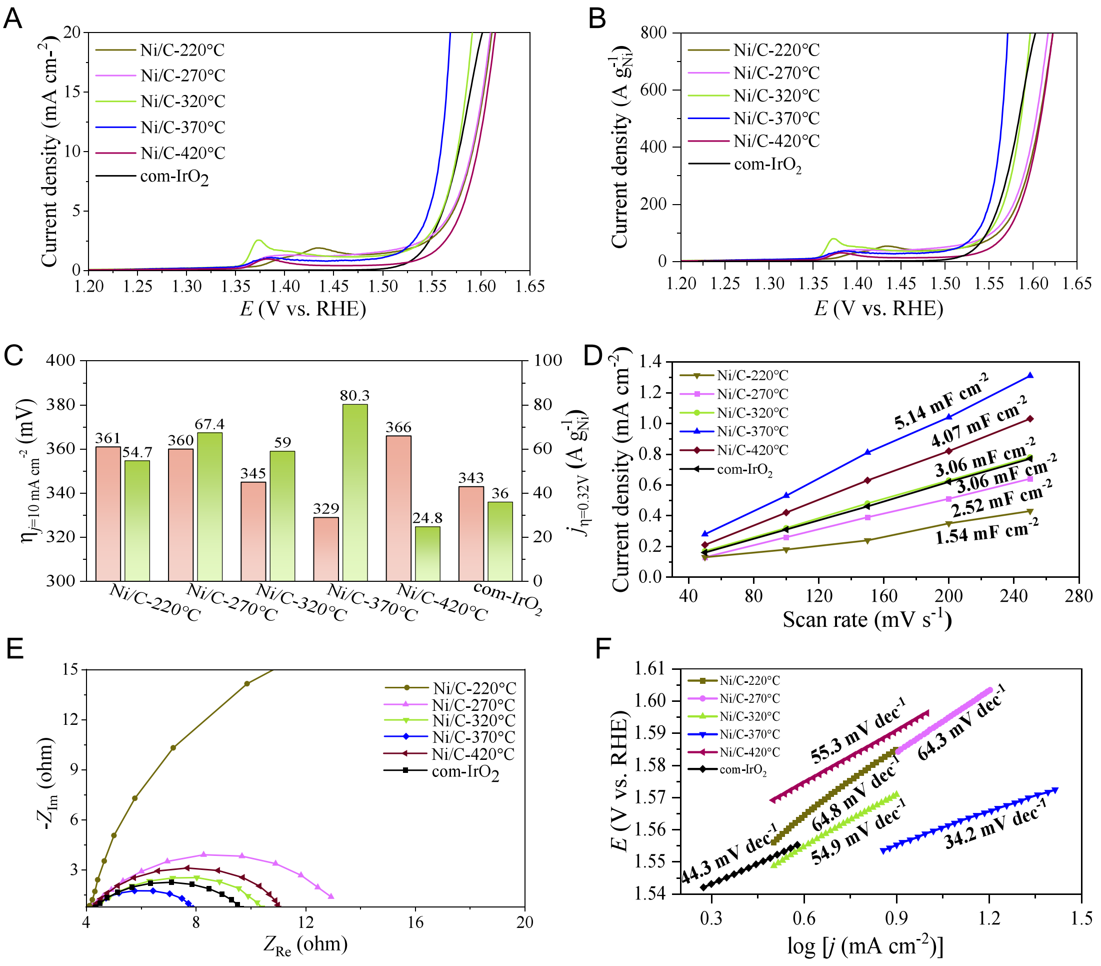

Figure 2. (A,B) OER polarization curves of the Ni/C-T and commercial IrO_2 catalyst (com-IrO_2) in O_2-saturated 1.0 M KOH solution where the current densities were normalized by geometric surface area of the electrode and the mass of total metal loaded on the electrode, respectively; (C) histograms showing the comparison of overpotentials for relevant catalysts at current density of 10 mA cm^{-2} and mass activities at 1.53 V vs RHE; (D) current densities at 0.574 V against scan rate for the Ni/C-T and com-IrO_2 catalyst; (E) Nyquist plots of the Ni/C-T and com-IrO_2 catalyst, in which the inset shows the equivalent circuit model; (F) Tafel plots derived from the polarization curves of corresponding catalysts.

to increase as the temperature continues to rise. This trend aligns with changes in the proportions of hcp phase in the carbon-supported Ni nanoparticles prepared at different temperatures. In specific, as disclosed by the XRD analyses, the Ni/C-370 °C has the highest proportion of hcp phase, manifesting that the hcp-Ni might have better OER catalytic activity than that of fcc-Ni.

It has been well documented that the electrochemically active surface areas (ESCAs) calculated from the double-layer capacitances (C_{dl}) could be used to estimate the intrinsic activity of the electrocatalysts for the OER. Figure S4 shows the cyclic voltammetry (CV) curves of the Ni/C-T and com-IrO_2 samples recorded at scan rates ranging from 50 to 250 mV s^{-1} in a non-Faradaic potential window of 0.524−0.624 V vs RHE. As shown in Figure 2D for the acquired C_{dl} values, the Ni/C-370° has the largest C_{dl} (5.14 mF cm^{-2}), which is higher than that of Ni/C-220 °C (1.54 mF cm^{-2}), Ni/C-270 °C (2.52 mF cm^{-2}), Ni/C-320 °C (3.06 mF cm^{-2}), Ni/C-420 °C (4.07 mF cm^{-2}), and com-IrO_2 (3.06 mF cm^{-2}), rationally reflecting that the Ni/C-370 °C sample has more active sites for the OER electrocatalysis. Notably, although the carbon-supported Ni nanoparticles synthesized at higher temperature (i.e., Ni/C-420 °C) have a larger average size (8.82 nm), their C_{dl} value can still reach 4.07 mF cm^{-2}. This may be attributed to the following reasons: (1) High temperature causes particle agglomeration, where multiple small particles fuse into larger ones. During this process, the surface of the particles may become irregular and rough; (2) thermal expansion at high temperature and subsequent contraction during cooling down process introduce stresses within and on the surface of particles, which may lead to the formation of cracks and other defects on the surface, thereby increasing surface roughness; (3) high temperatures encourage the accumulation of crystal defects, such as dislocations and vacancies, on the surface of the particles, which could create additional surface area by introducing irregularities and deviations from a perfectly smooth surface. A combination of the above-mentioned factors can explain why the effective surface area may not decrease significantly even as the Ni nanoparticles grow larger. On the contrary, in some cases, the ECSAs may actually increase due to the increase in roughness.

The kinetics of OER electrocatalysis on the Ni/C-T samples was investigated by electrochemical impedance spectroscopy (EIS). Figure 2E shows the Nyquist plots of these carbon-supported Ni catalysts, in which the Ni/C-370 °C has the smallest charge transfer resistance (R_{ct}) of 4.01 Ω, much lower than that of Ni/C-220 °C (45.92 Ω), Ni/C-270 °C (9.25 Ω), Ni/C-320 °C (5.62 Ω), Ni/C-420 °C (6.93 Ω), and com-IrO_2

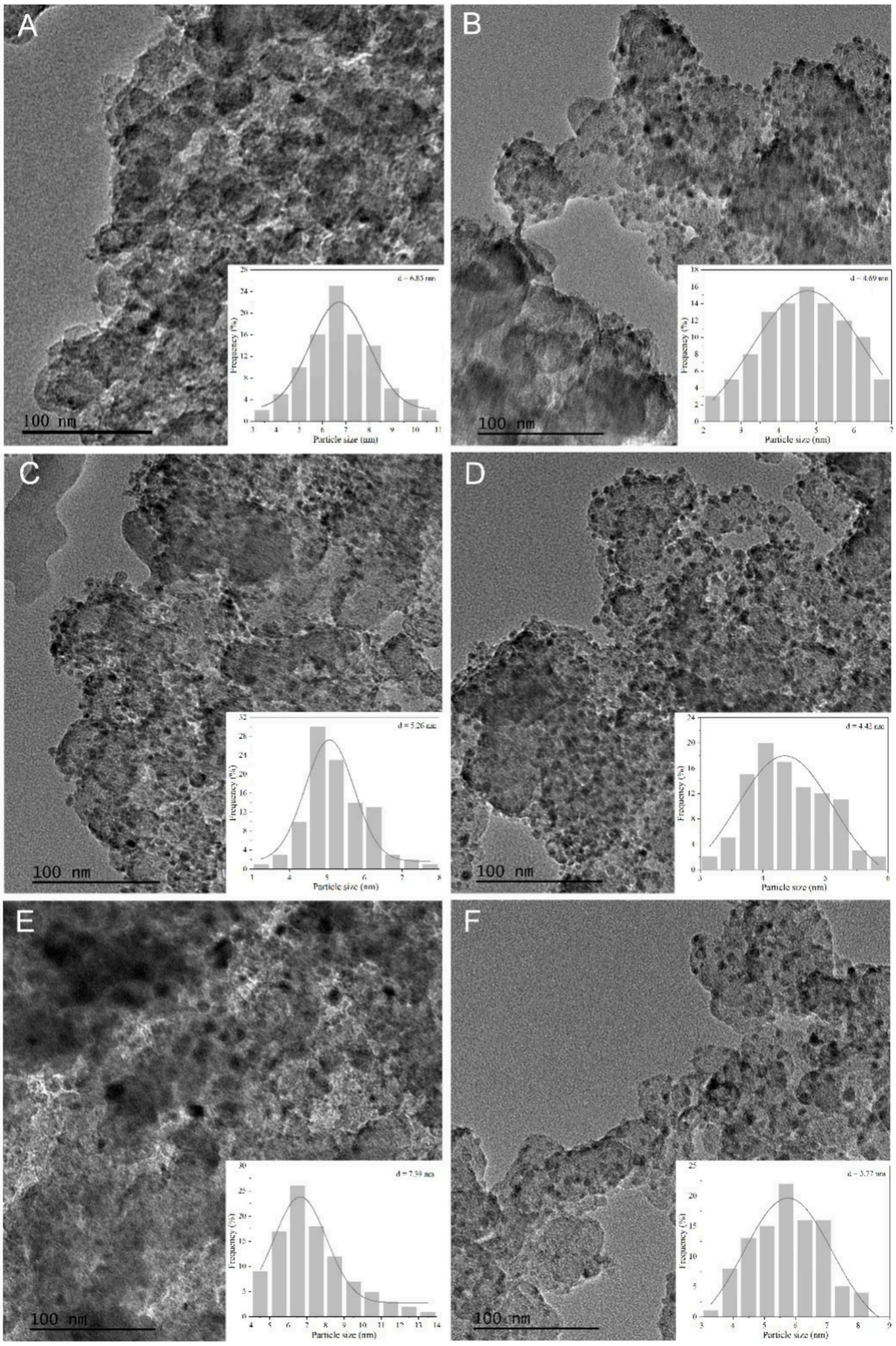

Figure 3. TEM images as well as corresponding particle size histograms of (A) $Ni_{94}Fe_6/C$, (B) $Ni_{72}Fe_{28}/C$, (C) $Ni_{58}Fe_{42}/C$, (D) $Ni_{43}Fe_{57}/C$, (E) $Ni_{13}Fe_{87}/C$, and (F) Fe/C, respectively.

(5.97 Ω), indicating that the carbon-supported Ni nanoparticles synthesized at 370 °C have the fastest reaction kinetics. In addition, Figure 2F shows a relatively lower Tafel slope of the Ni/C-370 °C sample (34.2 mV dec^{-1}) compared to that of Ni/C-220 °C (64.8 mV dec^{-1}), Ni/C-270 °C (64.3 mV dec^{-1}), Ni/C-320 °C (54.9 mV dec^{-1}), Ni/C-420 °C (55.3 mV dec^{-1}), and com-IrO_2 (44.3 mV dec^{-1}), thus verifying that Ni/C-370 °C favors the OER electrocatalysis under experimental conditions.

Syntheses and Characterizations of Bimetallic $Ni_{100-x}Fe_x/C$ Alloy Particles

Based on the investigations into the structure and the OER electrocatalysis of single-component Ni nanoparticles, we use Ni/C-370 °C as the matrix for Fe doping to prepare bimetallic NiFe alloys with different Ni/Fe molar ratios on the carbon substrate through a ball milling-Joule heating approach; that means the synthetic temperature for the $Ni_{100-x}Fe_x$ alloys was fixed at 370°, and only the feeding ratio of Ni and Fe precursors was changed. Therefore, in the sections that follow,

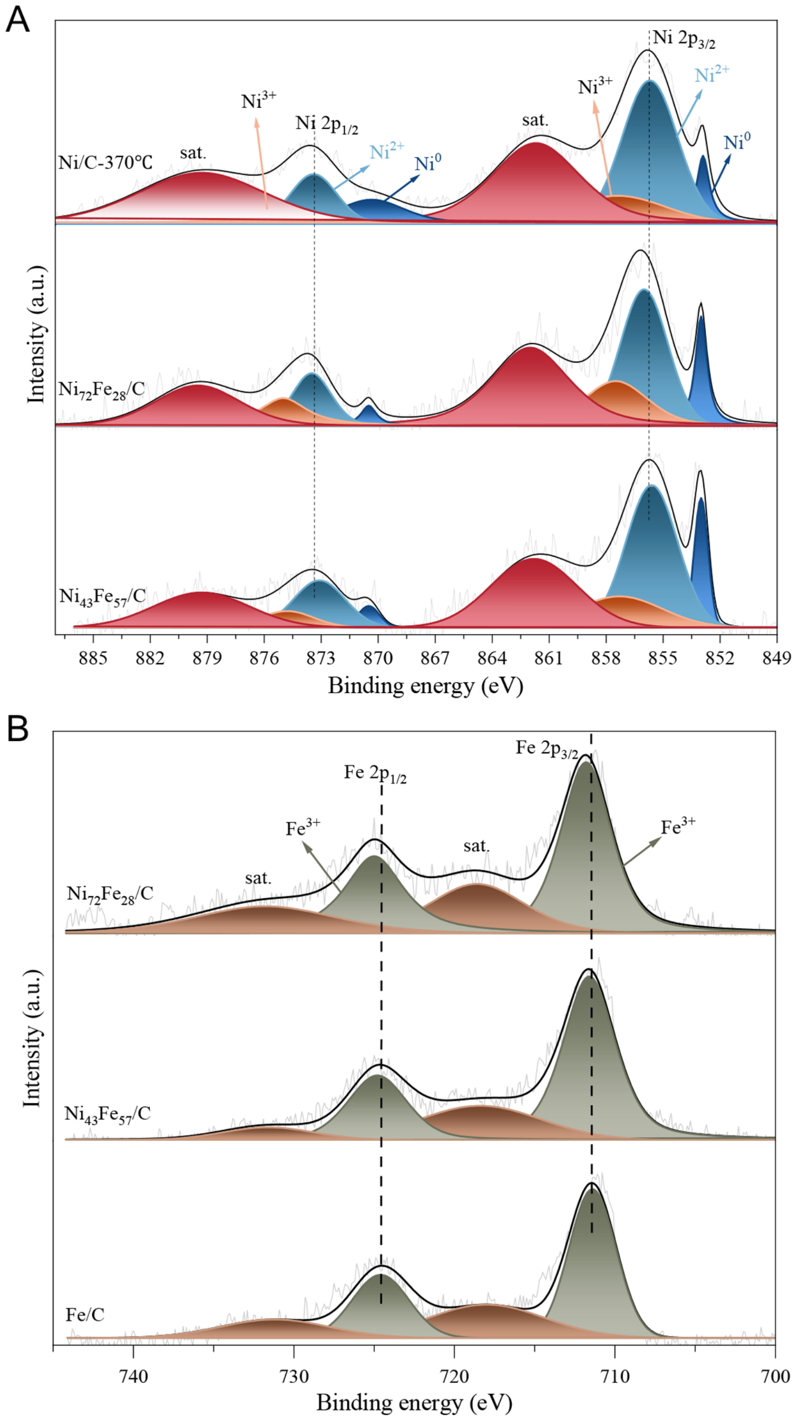

Figure 4. 2p XPS spectra of (A) Ni in single-component Ni/C-370 °C, $Ni_{72}Fe_{28}$/C, and $Ni_{43}Fe_{57}$/C samples; (B) the 2p XPS spectra of Fe in $Ni_{72}Fe_{28}$/C, $NNi_{43}Fe_{57}$/C and single-component Fe/C samples.

we will label the as-prepared carbon-supported alloy samples as $Ni_{100-x}Fe_x$/C, and we will no longer display the temperature value.

XRD was once again used first to analyze the structure of the binary NiFe samples obtained by ball milling-Joule heating approach under hydrogen reduction atmosphere. The XRD patterns of the binary NiFe samples at different Ni/Fe feeding ratios are shown in Figure S5, in which the Ni/C-370 °C matrix and single-component Fe/C sample are also included for convenient comparison. Apparently, the XRD patterns of binary NiFe samples have only a set of homogeneous diffraction peaks that shift gradually to lower 2θ values as the Fe content increases, indicating the formation of alloy nanoparticles. Also as observed, unfortunately, although we select the temperature that leads to the highest hcp proportion in single-component Ni/C sample, the as-produced bimetallic NiFe alloy samples with different Ni/Fe ratios supported on carbon substrate only display the fcc phase, as evinced by the diffraction peaks at 2θ at ca. 43.8°−44.5° and ca. 50.9°−51.9°, which correspond to the (111) and (200) planes of fcc

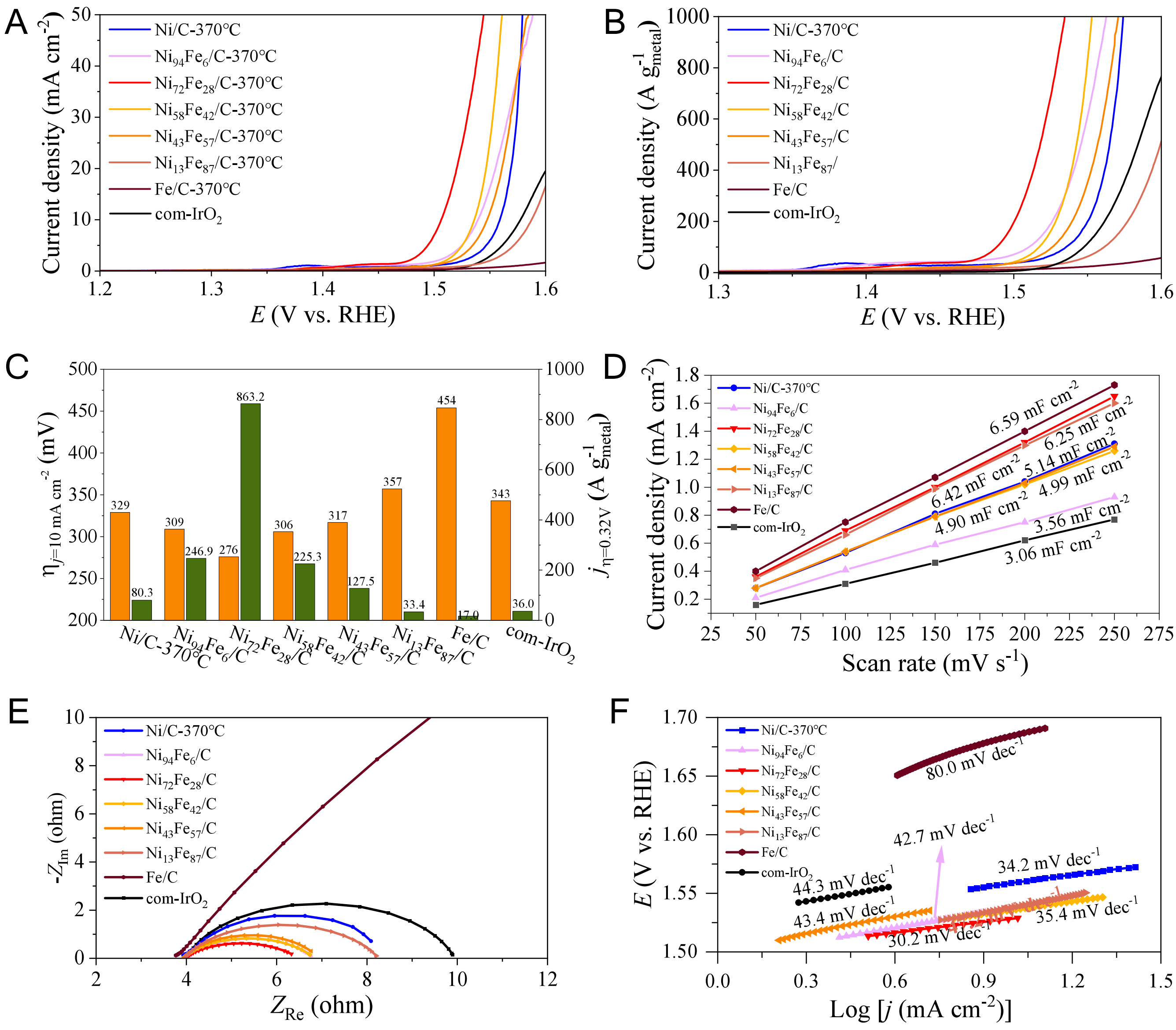

Figure 5. (A,B) OER polarization curves of the $Ni_{100-x}Fe_x/C$ as well as the Ni/C-370 °C and com-IrO_2 catalyst in O_2-saturated 1.0 M KOH solution where the current densities were normalized by electrode surface area of the and the total mass loading, respectively; (C) histograms showing the comparison of overpotentials for relevant catalysts at current density of 10 mA cm^{-2} and mass activities at 1.53 V vs RHE; (D) current densities at 0.574 V against scan rate for the $Ni_{100-x}Fe_x/C$ as well as the Ni/C-370 °C and com-IrO_2 catalyst; (E) Nyquist plots of the $Ni_{100-x}Fe_x/C$ as well as the Ni/C-370 °C and com-IrO_2 catalyst, in which the inset shows the equivalent circuit model; (F) Tafel plots derived from the polarization curves of corresponding catalysts.

structure, revealing that the Fe doping has a significant effect on the Ni phase during the formation of alloy particles. Notably, for the single-component Fe/C sample, Figure S5 shows that most of the Fe element is in an oxidized state, meaning that Fe is very easy to oxidize.

The morphology and size of the $Ni_{100-x}Fe_x/C$ samples were observed by using TEM. Figure 3A–F clearly show that the $Ni_{100-x}Fe_x$ alloy particles uniformly distribute on the carbon substrate, with average sizes ranging from ca. 4 to 8 nm. Notably, the morphology of the $Ni_{100-x}Fe_x$ alloy particles with different Ni/Fe ratios is very similar, implying that the changes in the proportion of Fe element have a negligible impact on the morphology of the final alloy product. The $Ni_{72}Fe_{28}/C$ was taken as a typical sample to conduct high-resolution TEM (HRTEM) characterization of the alloy particles, which reveals their crystalline nature, with a lattice spacing of 1.82 Å in $Ni_{72}Fe_{28}/C$ that corresponds to the (200) plane of the cubic Ni_3Fe phase, as seen in Figure S6A. In addition, the HAADF-STEM image and corresponding energy-dispersive X-ray spectroscopy (EDX)-based element maps over a large area of the $Ni_{72}Fe_{28}/C$ sample were obtained (Figure S6B1–B4), from which we do not succeed to analyze the Ni and Fe distributions by spotting on one single $Ni_{72}Fe_{28}$ particle due to its small size. Fortunately, the element maps in Figure S6 reveal a consistent distribution of Ni and Fe on the carbon substrate, which can serve as a strong evidence of the formation of binary NiFe alloys.

X-ray photoelectron spectroscopy (XPS) was used to examine the chemical states on the surfaces of the $Ni_{100-x}Fe_x/C$ samples, which are closely associated with their OER electrocatalysis. Here, we chose $Ni_{72}Fe_{28}/C$ and $Ni_{43}Fe_{57}/C$ as two typical samples to conduct the XPS surveys and benchmarked them against single-component Ni/C-370 °C and Fe/C for studying the possible electronic interactions between Ni and Fe atoms. For a wide XPS spectrum of $Ni_{72}Fe_{28}$/C, the presence of Ni, Fe, C, and O elements could be confirmed, as shown in Figure S7. Then as shown in Figure 4A, the high-resolution Ni 2p XPS spectra of the $Ni_{72}Fe_{28}$/C, $Ni_{43}Fe_{57}$/C, and Ni/C-370 °C samples exhibit the Ni $2p_{3/2}$ and Ni $2p_{1/2}$ regions, each of which includes four peaks. In detail, the doublet at binding energies of ca. 852.9−853.5 eV and ca. 870.2−871.0 eV is attributed to zerovalent Ni metal, while the doublets at ca. 855.7−856.2 eV and 873.4−873.6 eV, and at ca. 857.5−857.8 eV and 874.8−875.2 eV are assigned to Ni^{2+} and Ni^{3+} species, respectively, with satellite doublet at ca. 861.7−862.3 eV and ca. 879.3−879.8 eV. Obviously, the binding energies of Ni 2p electrons for the $Ni_{72}Fe_{28}$/C and $Ni_{43}Fe_{57}$/C are higher than those of the Ni/C-370 °C, suggesting that the Fe dopant can modulate the Ni electronic structure.[48] Correspondingly, as seen in Figure 4B, the Fe 2p XPS spectra for the $Ni_{72}Fe_{28}$/C, $Ni_{43}Fe_{57}$/C and Fe/C samples can all be deconvoluted into two doublets, i.e. the binding energies at ca. 711.4−711.9 eV and at ca. 724.6−725.0 eV for Fe^{3+} $2p_{3/2}$ and $2p_{1/2}$ peak, respectively, accompanied by two broad satellite doublet at ca. 718.0−718.6 eV and 731.2−731.8 eV, indicating that the Fe component on the particle surfaces is primarily present in Fe^{3+} form.

When Ni^{2+} couples with Fe^{3+}, charges might partially transfer from the Ni^{2+} to Fe^{3+}, generating $Ni^{3+\delta}$ species with a higher valence state. Also, the electronic interaction between the Ni^{2+} and Fe^{3+} species results in higher binding energies for the Fe^{3+} species in the $Ni_{72}Fe_{28}$/C and $Ni_{43}Fe_{57}$/C samples relative to those of Fe^{3+} in the single-component Fe/C sample (Figure 4B). The increase in Ni valence would promote charge transfer between the $Ni_{100-x}Fe_x$/C and OH^- species through enhancement of adsorption of the latter, thereby helping to improve the OER performance. We also probed the O 1s XPS spectra for the $Ni_{72}Fe_{28}$/C, $Ni_{43}Fe_{57}$/C, and Ni/C-370 °C samples. As shown by Figure S8, all the O 1s XPS spectrum of the $Ni_{72}Fe_{28}$/C, $Ni_{43}Fe_{57}$/C, and Ni/C-370 °C samples can be fitted by three peaks located at ca. 530.1−530.6, 532.2, and 533.8 eV corresponding to oxygen in lattice oxides (Ni−O/Fe-O), metal hydroxides (M−OH), and surface adsorbed water (H_2O_{ads}), respectively.[49] In specific, the binding energy of the lattice oxygen in the $Ni_{72}Fe_{28}$/C and $Ni_{43}Fe_{57}$/C shifts by 0.5 eV compared to that in the Ni/C-370 °C sample, also indicating higher metal oxidation states on the alloy surface.[50] This shift could be due to charge transfer between Ni and Fe upon alloying, which affects the binding energy of the 1s electrons.

Electrocatalytic Evaluation of the $Ni_{100-x}Fe_x$/C for OER

Using the standard three-electrode configuration, we systematically evaluated the OER performances of the $Ni_{100-x}Fe_x$/C samples in an O_2-saturated 1 M KOH and compared them with the single-component Ni/C-370 °C and commercial IrO_2 catalyst (com-IrO_2). The actual metal (Ni + Fe) mass loadings on the carbon substrate for all $Ni_{100-x}Fe_x$/C samples were also determined by ICP-AES (Table S1).

Figure 5A and B show the linear sweep voltammetry (LSV) curves of the $Ni_{100-x}Fe_x$/C samples as well as the Ni/C-370 °C and com-IrO_2 normalized by electrode area and total metal mass loading, respectively, in which the $Ni_{72}Fe_{28}$/C displays the best OER activity, with the η_{10} of only 276 mV, which is lower than that of the Ni/C-370 °C (302 mV), $Ni_{94}Fe_6$/C (309 mV), $Ni_{58}Fe_{42}$/C (306 mV), $Ni_{43}Fe_{57}$/C (317 mV), $Ni_{13}Fe_{87}$/C (357 mV), Fe/C (454 mV), commercial IrO_2 (343 mV), and many other reported OER electrocatalysts (Table S2). It is noteworthy that the peak around 1.38 V vs RHE observed for the $Ni_{100-x}Fe_x$/C samples corresponds to the transformation of $Ni(OH)_2$ to NiOOH.[51] In addition, the mass-based activity of the $Ni_{72}Fe_{28}$/C catalyst reaches 863.2 A g^{-1} at 1.53 V vs RHE, which is also the highest value among the catalysts tested, as those compared in Figure 5C. It has been reported that the presence of Fe lowers the reaction free energy for the conversion of Ni^{2+} to $Ni^{3+\delta}$,[36,52] where the $Ni^{3+\delta}$ is a key active species for OER catalysis. Therefore, forming an alloy with iron can improve the performance of Ni in catalyzing the OER. The high OER electrocatalysis of $Ni_{72}Fe_{28}$/C is easy to understand. When the Ni content is high, the small Fe amount in the alloy is insufficient to produce more active $Ni^{3+\delta}$ species; however, when the Fe content in the alloy is too high, the dilution effect it brings can also lead to insufficient Ni active sites on the catalyst surface. Therefore, only at an appropriate Ni/Fe ratio can the NiFe alloy particles exhibit the best OER catalytic performance.

To further investigate the key active species on the surface of the $Ni_{72}Fe_{28}$/C sample and the critical reaction intermediates during the OER process, potential-dependent in situ Raman spectroscopy was performed. The in situ Raman spectra of the $Ni_{72}Fe_{28}$/C anode collected under multiple potential steps in 1.0 M KOH are shown in Figure S9. As observed, during the OER process in 1.0 M KOH, the Raman spectra in the range from open-circuit voltage to 1.22 V exhibit two characteristic peaks at 441 and 512 cm^{-1}, corresponding to the E_g bending vibration and A_{1g} stretching vibration of the Ni−O bond in $Ni(OH)_2$, respectively. The Raman peak at 680 cm^{-1} can be attributed to the Fe−O bond in α-FeOOH, indicative of iron hydroxide nanoparticles.[53] When the applied potential exceeds 1.30 V vs RHE, characteristic peaks of NiOOH can be observed at 466 and 545 cm^{-1}, corresponding to the E_g bending vibration and A_{1g} stretching vibration of Ni^{3+}-O in NiO_6 units,[54] respectively. These peaks indicate the transformation from $Ni(OH)_2$ to NiOOH, driven by the applied potential, which is consistent with the observation for the oxidation peaks in the LSV curve of the $Ni_{72}Fe_{28}$/C during OER testing, suggesting that the NiOOH is the key active species catalyzing the OER.[50] The intensity of the dual peaks increases with rising potential and stabilizes at 1.42 V vs RHE, suggesting that the $Ni(OH)_2$ has fully transformed into NiOOH. Simultaneously, as the potential increases, the characteristic peak of α-FeOOH gradually disappears, possibly due to the dissolution of Fe at the catalyst-electrolyte interface.[38] After the transformation from $Ni(OH)_2$ to NiOOH, the E_g bending vibration peak of the latter becomes more intense than the A_{1g} stretching vibration peak, indicating a stronger bending vibration and potential changes in its crystal structure. The shortening of the Ni−O bond length can lower the activation energy, thereby enhancing the OER activity. Additionally, strengthening the Ni−O bond improves the durability of the catalyst by reducing structural changes and deactivation during the electrochemical reaction.

Figure S10 shows the cyclic voltammetry (CV) curves of the alloy $Ni_{100-x}Fe_x$/C samples at scan rates of 50−250 mV s^{-1} under the non-Faradaic potential window of 0.524−0.624 V vs RHE, which can be used to calculate their double-layer capacitances (C_{dl}) for evaluation of the ECSAs. As marked in Figure 5D, the C_{dl} of the $Ni_{72}Fe_{28}$/C is 6.42 mF cm^{-2}, slightly

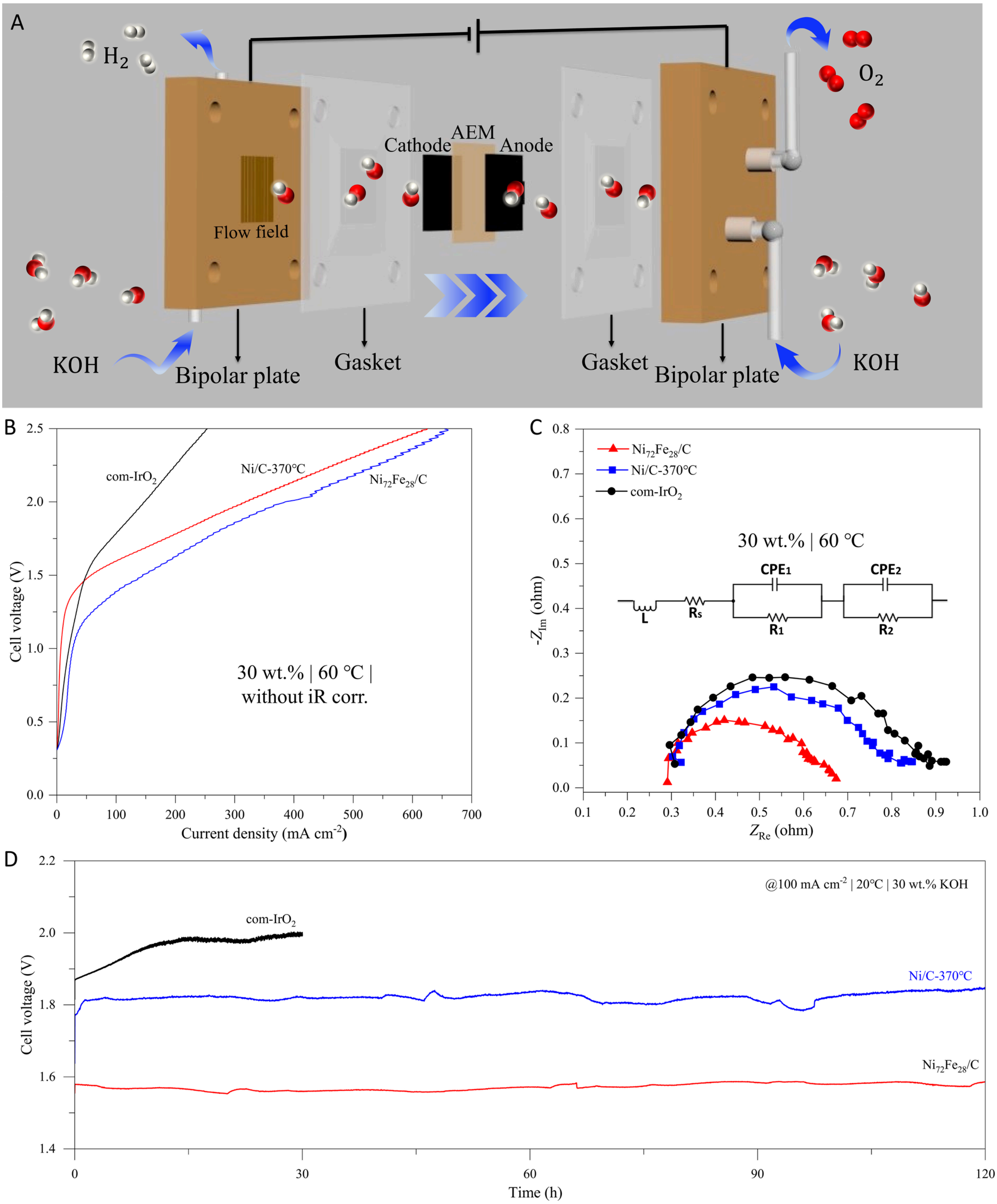

Figure 6. (A) Schematic diagram showing the alkaline water electrolysis, in which carbon papers were used as the liquid/gas diffusion layers for both cathode and anode; (B) polarization curves of the Pt/C∥Ni$_{72}$Fe$_{28}$/C, Pt/C∥Ni/C-370 °C and Pt/C∥com-IrO$_2$ in 30 wt % KOH at 60 °C; (C) Nyquist plots of the AEMWEs equipped with different catalyst as the anode in 30 wt % KOH at 60 °C; (D) cell voltage−time plots for the Pt/C∥Ni$_{72}$Fe$_{28}$/C, PtC/CP∥Ni/C-370 °C and Pt/C∥com-IrO$_2$ at a constant current density of 100 mA cm^{-2} at 60 °C.

higher than or comparable to that of carbon-supported NiFe alloy particles at other Ni/Fe ratios, also supporting its better electrocatalysis for the OER. Notably, although a single-component Fe/C sample has relatively higher C_{dl} (6.59 mF cm^{-2}), the easy oxidation nature of Fe makes it difficult to apply in the electrocatalysis of the OER.

The Nyquist plots shown in Figure 5E evince that the $Ni_{72}Fe_{28}/C$ sample has the smallest arc diameter, meaning its fastest electron transfer rate at the catalyst-electrolyte interface. In detail, the R_{ct} of the $Ni_{72}Fe_{28}/C$ sample is 2.26 Ω, followed by 2.77 Ω for $Ni_{94}Fe_6/C$, 2.82 Ω for $Ni_{58}Fe_{42}/C$, 2.85 Ω for $Ni_{43}Fe_{57}/C$, 4.25 Ω for $Ni_{13}Fe_{87}/C$, and 76.88 Ω for Fe/C, respectively. Besides, as shown in Figure 5F, the Tafel slope of the $Ni_{72}Fe_{28}/C$ is 30.2 mV dec^{-1}, smaller than that of the carbon-supported NiFe alloys at other Ni/Fe ratios, Ni/C-370 °C and com-IrO_2 as well as most reported Ni-based electrocatalysts (Table S2). This indicates that the $Ni_{72}Fe_{28}/C$ possesses a faster kinetic process that is favorable for electron transfer during the OER electrocatalysis.

The stability of the $Ni_{72}Fe_{28}/C$ sample was evaluated by using an electrochemical overall water splitting test in a two-electrode electrolyzer with a scan rate of 5 mV s^{-1} in 1 M KOH. Figure S11A shows the schematic setup of the two-electrode electrolyzer, in which the $Ni_{72}Fe_{28}/C$, Ni/C-370 °C, or com-IrO_2 catalyst was spray-coated onto carbon paper as the anode, while Pt/C from Johnson Matthey was used as the cathode, with a metal loading of 2 mg cm^{-2}. As shown in Figure S11B, the Pt/C|| $Ni_{72}Fe_{28}/C$ system achieves a voltage of only 1.485 V at the current density of 10 mA cm^{-2} (without *iR* compensation), outperforming the Pt/C||Ni/C-370 °C and Pt/C||com-IrO_2 systems and a number of other reported two-electrode water splitting systems (Table S3). The long-term stability of the $Ni_{72}Fe_{28}/C$ is featured by Figure S11C for the chronopotentiometry at the current density of 10 mA cm^{-2}. As shown, after a 20-h durability test, the $Ni_{72}Fe_{28}/C$ sample still maintain lower voltage than that of the Ni/C-370 °C and com-IrO_2 catalyst, indicating its better stability for OER.

The two-electrode electrolyzer here can even be run by a commercial AA battery with a nominal voltage of 1.5 V, in which the bubbles staying on the electrode are clearly visible (Figure S12). In a sealed H-type electrolyzer, the overall water splitting driven by the Pt/C|| $Ni_{72}Fe_{28}/C$ system was performed, and H_2 and O_2 produced at the anode and cathode were collected by the drainage method (Figure S13A). Figure S13B,C show the volumes of H_2 and O_2 gas collected at specific time intervals, while Figure S13D shows the gas bubbles generated on the electrode. The volume changes at different times are plotted in Figure S13E, in which the 2/1 volume ratio H_2/O_2 definitely confirms that the gases are produced from water splitting.

Performance in the Anion Exchange Membrane Water Electrolyzers (AEMWEs)

We built an anion exchange membrane water electrolyzer (AEMWE) to investigate the performance of the $Ni_{72}Fe_{28}/C$ in practical devices, as schematically shown by Figure 6A, in which the $Ni_{72}Fe_{28}/C$ particles were coated on carbon paper (CP) by an ultrasonic precision sprayer with the loading of 1.3 mg cm^{-2} as the anode catalyst. This was compared with Ni/C-370 °C and commercial IrO_2 as the anode catalysts with the same mass loadings. The membrane electrode assembly (MEA) was prepared using an anion exchange membrane and the same loading of 20% Pt/C as the cathode catalyst. At 60 °C, a 1 M KOH solution was pumped into the device at a flow rate of 4.8 mL min^{-1} from both the anode and cathode, with an active area of 4 cm^2. In particular, the Pt/C|| $Ni_{72}Fe_{28}/C$ system achieves a cell voltage of only 1.39 V at the current density of 100 mA cm^{-2}, lower than that of Ni/C-370 °C, com-IrO_2, and some other reported cells (Figure 6B and Table S4). It is noteworthy that the cell performance is greatly affected by temperature and electrolyte concentration (Figure S14) and the high temperature and electrolyte concentration help to boost the performance. EIS tests were conducted at 1.9 V to probe the resistance in AEMWEs.[55] Figure 6C shows that the cell resistance for $Ni_{72}Fe_{28}/C$ has the smallest charge transfer resistance (0.16 Ω cm^2), also meaning that its good performance for overall water splitting.

In practical applications, the stability of a catalyst is often more crucial than its activity. In this regard, the durability of the Pt/C||$Ni_{72}Fe_{28}/C$ system for alkaline water electrolysis was evaluated at a current density of 100 mA cm^{-2} (see Figure S15 for the testing setup and supplementary video for its dynamic operation). As shown in Figure 6D, the Pt/C||$Ni_{72}Fe_{28}/C$ system maintains stable for over 120 h in a 30 wt % KOH solution, with a voltage increase rate of 69.2 μV h^{-1}, which is much lower than that of the Pt/C||com-IrO_2 system (4174.0 μV h^{-1}). Also, the Pt/C||Ni/C-370 °C system exhibits good stability, with the voltage increasing by only 71.2 mV after 120-h operation. All electrochemical evaluations indicate that the $Ni_{72}Fe_{28}/C$ synthesized by ball milling-Joule heating method is a highly active and durable OER catalyst, suitable for practical applications in AEMWEs.

Coupling Joule heating with solid-phase ball milling offers several notable advantages in the preparation of metal nanoparticles, including: (1) Joule heating enables rapid heating and cooling, facilitating the formation of fine particles; (2) ball milling allows for solid-phase mixing, ensuring uniform distribution of precursors on the substrate surfaces; (3) it is easy to adjust the stoichiometric ratio of the final product by altering the precursor ratios; (4) the surfaces of the final particles are clean, which favors the sufficient exposure of active sites. However, this preparation method also has significant drawbacks. First, we have observed that the selected metal precursors often undergo sublimation during rapid heating, resulting in considerable waste. Additionally, due to the limited adjustable parameters during the synthesis process, it is challenging to control the size, morphology, and structure of the final particles. In light of this, we hypothesize that combining the rapid heating and cooling characteristics of Joule heating with the advantages of wet chemistry methods, which offer more adjustable parameters, may optimize the particle size, morphology, and structure, further enhancing the electrocatalytic performance.

■ CONCLUSION

In summary, we have developed an efficient Joule heating coupled ball milling method for preparing $Ni_{100-x}Fe_x$ alloy nanoparticles on a carbon substrate as high-efficiency and stable OER electrocatalysts. By simply mixing the precursors and carbon substrate through ball milling and subsequently subjecting them to Joule heating, carbon-supported alloy nanoparticles with fine sizes and uniform distribution are rapidly formed. In specific, the single-component Ni/C nanoparticles (i.e., $x = 0$), synthesized by this ball milling-Joule heating strategy have both fcc and hcp crystal phases, and the proportion of the latter reaches its maximum at 370 °C, which endows the Ni/C nanoparticles synthesized at 370 °C with better OER activity than that of Ni/C samples synthesized at other temperatures. In addition, an optimal electronic interaction between Ni and Fe equips the

$Ni_{100-x}Fe_x/C$ nanoparticles at the Ni/Fe ratio of 72/28 ($Ni_{72}Fe_{28}/C$) with the best OER electrocatalysis, with a low overpotential of only 276 mV at a current density of 10 mA cm^{-2}. Further, under simulated industrial electrolysis conditions (30 wt % KOH at 60 °C), a two-electrode alkaline electrolyzer assembled with $Ni_{72}Fe_{28}/C$ at the anode and commercial Pt/C at the cathode ($Ni_{72}Fe_{28}/C \| Pt/C$) requires only a voltage of 1.39 V to deliver the current density of 100 mA cm^{-2}, along with an excellent 120-h durability at the current density of 100 mA cm^{-2}. This study therefore provides a fast and economical approach for producing high-efficiency electrocatalysts for the practical anion exchange membrane water electrolysis.

ASSOCIATED CONTENT

Supporting Information

The Supporting Information is available free of charge at https://pubs.acs.org/doi/10.1021/acsaenm.4c00591.

Experimental details, tables showing actual atomic ratio of the as-prepared atomic steps, mass loading of the catalysts and comparison of electrocatalytic activity between the carbon-supported $Ni_{100-x}Fe_x$ alloy nanoparticles in this study and some recently reported transition metal-based catalysts for OER in an alkaline electrolyte, and Supporting Information including further details of TEM images, size distribution histogram, surface valence spectra, in situ Raman spectra, electrochemical measurements, water splitting setup, and additional references (PDF)

Video showing the dynamic operation of the water splitting setup (MP4)

AUTHOR INFORMATION

Corresponding Authors

Guozhu Chen − *School of Chemistry and Chemical Engineering, University of Jinan, Jinan 250022, China;* orcid.org/0000-0002-3976-1240; Email: chm_chengz@ujn.edu.cn

Shaonan Tian − *State Key Laboratory of Mesoscience and Engineering, Institute of Process Engineering, Chinese Academy of Sciences, Beijing 100190, China;* Email: sntian@ipe.ac.cn

Jun Yang − *State Key Laboratory of Mesoscience and Engineering, Institute of Process Engineering, Chinese Academy of Sciences, Beijing 100190, China; Center of Materials Science and Optoelectronics Engineering, University of Chinese Academy of Sciences, Beijing 100049, China;* orcid.org/0000-0002-8993-0655; Email: jyang@ipe.ac.cn

Lin Xu − *School of Chemistry and Materials Science, Jiangsu Key Laboratory of New Power Batteries, Jiangsu Collaborative Innovation Centre of Biomedical Functional Materials, Nanjing Normal University, Nanjing 210023, China;* Email: xulin001@njnu.edu.cn

Authors

Li Zhang − *School of Chemistry and Chemical Engineering, University of Jinan, Jinan 250022, China; State Key Laboratory of Mesoscience and Engineering, Institute of Process Engineering, Chinese Academy of Sciences, Beijing 100190, China*

Mengyuan Ma − *State Key Laboratory of Mesoscience and Engineering, Institute of Process Engineering, Chinese Academy of Sciences, Beijing 100190, China; Center of Materials Science and Optoelectronics Engineering, University of Chinese Academy of Sciences, Beijing 100049, China*

Zhenya Hu − *State Key Laboratory of Mesoscience and Engineering, Institute of Process Engineering, Chinese Academy of Sciences, Beijing 100190, China; Center of Materials Science and Optoelectronics Engineering, University of Chinese Academy of Sciences, Beijing 100049, China*

Hui Liu − *State Key Laboratory of Mesoscience and Engineering, Institute of Process Engineering, Chinese Academy of Sciences, Beijing 100190, China*

Dong Chen − *State Key Laboratory of Mesoscience and Engineering, Institute of Process Engineering, Chinese Academy of Sciences, Beijing 100190, China;* orcid.org/0000-0002-9280-2865

Complete contact information is available at: https://pubs.acs.org/10.1021/acsaenm.4c00591

Author Contributions

[§]L.Z. and M.M. contributed equally to this work.

Notes

The authors declare no competing financial interest.

ACKNOWLEDGMENTS

We gratefully acknowledge the financial supports from the National Natural Science Foundation of China (22272179, 22075290), CAS Project for Young Scientists in Basic Research (YSBR-044), the Energy Revolution S&T Program of Yulin Innovation Institute of Clean Energy (E411060705), and State Key Laboratory of Mesoscience and Engineering, Institute of Process Engineering, Chinese Academy of Sciences (MESO-23-A06, MESO-24-A01).

REFERENCES

(1) Zhang, Q.; Chen, W.; Chen, G.; Huang, J.; Song, C.; Chu, S.; Zhang, R.; Wang, G.; Li, C.; Ostrikov, K. K. Bi-Metallic Nitroxide Nanodot-Decorated Tri-Metallic Sulphide Nanosheets by on-Electrode Plasma-Hydrothermal Sprouting for Overall Water Splitting. *Appl. Catal. B: Environ.* **2020**, *261*, No. 118254.

(2) Ding, X.; Uddin, W.; Sheng, H.; Li, P.; Du, Y.; Zhu, M. Porous Transition Metal Phosphides Derived from Fe-Based Prussian Blue Analogue for Oxygen Evolution Reaction. *J. Alloys Compd.* **2020**, *814*, No. 152332.

(3) Zhang, K.; Zou, R. Advanced Transition Metal-Based OER Electrocatalysts: Current Status, Opportunities, and Challenges. *Small* **2021**, *17*, No. 2100129.

(4) Feng, J.; Ye, S.; Xu, H.; Tong, Y.; Li, G. Design and Synthesis of $FeOOH/CeO_2$ Heterolayered Nanotube Electrocatalysts for the Oxygen Evolution Reaction. *Adv. Mater.* **2016**, *28*, 4698−4703.

(5) Huang, Y.; Chong, X.; Liu, C.; Liang, Y.; Zhang, B. Boosting Hydrogen Production by Anodic Oxidation of Primary Amines over a NiSe Nanorod Electrode. *Angew. Chem., Int. Ed.* **2018**, *57*, 13163−13166.

(6) Zhao, Z. L.; Wang, Q.; Huang, X.; Feng, Q.; Gu, S.; Zhang, Z.; Xu, H.; Zeng, L.; Gu, M.; Li, H. Boosting the Oxygen Evolution Reaction Using Defect-Rich Ultra-Thin Ruthenium Oxide Nanosheets in Acidic Media. *Energy Environ. Sci.* **2020**, *13*, 5143−5151.

(7) Seitz, L. C.; Dickens, C. F.; Nishio, K.; Hikita, Y.; Montoya, J.; Doyle, A.; Kirk, C.; Vojvodic, A.; Hwang, H. Y.; Norskov, J. K.; Jaramillo, T. F. A Highly Active and Stable $IrO_x/SrIrO_3$ Catalyst for the Oxygen Evolution Reaction. *Science* **2016**, *353*, 1011−1014.

(8) Huang, W.; Wang, H.; Zhou, J.; Wang, J.; Duchesne, P. N.; Muir, D.; Zhang, P.; Han, N.; Zhao, F.; Zeng, M.; Zhong, J.; Jin, C.; Li, Y.; Lee, S.-T.; Dai, H. Highly Active and Durable Methanol Oxidation Electrocatalyst Based on the Synergy of Platinum−Nickel Hydroxide−Graphene. *Nat. Commun.* **2015**, *6*, 10035.

(9) Li, J.; Luo, Z.; He, F.; Zuo, Y.; Zhang, C.; Liu, J.; Yu, X.; Du, R.; Zhang, T.; Infante-Carrió, M. F.; Tang, P.; Arbiol, J.; Llorca, J.; Cabot, A. Colloidal Ni−Co−Sn Nanoparticles as Efficient Electrocatalysts for the Methanol Oxidation Reaction. *J. Mater. Chem. A* **2018**, *6*, 22915−22924.

(10) Wang, Y.; Zhu, Y.; Zhao, S.; She, S.; Zhang, F.; Chen, Y.; Williams, T.; Gengenbach, T.; Zu, L.; Mao, H.; Zhou, W.; Shao, Z.; Wang, H.; Tang, J.; Zhao, D.; Selomulya, C. Anion Etching for Accessing Rapid and Deep Self-Reconstruction of Precatalysts for Water Oxidation. *Matter* **2020**, *3*, 2124−2137.

(11) Kim, J. S.; Kim, B.; Kim, H.; Kang, K. Recent Progress on Multimetal Oxide Catalysts for the Oxygen Evolution Reaction. *Adv. Energy Mater.* **2018**, *8*, No. 1702774.

(12) Jia, X.; Zhang, X.; Zhao, J.; Zhao, Y.; Zhao, Y.; Waterhouse, G. I. N.; Shi, R.; Wu, L.-Z.; Tung, C.-H.; Zhang, T. Ultrafine Monolayer Co-Containing Layered Double Hydroxide Nanosheets for Water Oxidation. *J. Energy Chem.* **2019**, *34*, 57−63.

(13) Gong, M.; Li, Y.; Wang, H.; Liang, Y.; Wu, J. Z.; Zhou, J.; Wang, J.; Regier, T.; Wei, F.; Dai, H. An Advanced Ni−Fe Layered Double Hydroxide Electrocatalyst for Water Oxidation. *J. Am. Chem. Soc.* **2013**, *135*, 8452−8455.

(14) Kim, B.; Kabiraz, M. K.; Lee, J.; Choi, C.; Baik, H.; Jung, Y.; Oh, H.-S.; Choi, S.-I.; Lee, K. Vertical-Crystalline Fe-Doped *β*-Ni Oxyhydroxides for Highly Active and Stable Oxygen Evolution Reaction. *Matter* **2021**, *4*, 3585−3604.

(15) Peng, L.; Yang, N.; Yang, Y.; Wang, Q.; Xie, X.; Sun-Waterhouse, D.; Shang, L.; Zhang, T.; Waterhouse, G. I. N. Atomic Cation-Vacancy Engineering of NiFe-Layered Double Hydroxides for Improved Activity and Stability towards the Oxygen Evolution Reaction. *Angew. Chem., Int. Ed.* **2021**, *60*, 24612−24619.

(16) Callejas, J. F.; McEnaney, J. M.; Read, C. G.; Crompton, J. C.; Biacchi, A. J.; Popczun, E. J.; Gordon, T. R.; Lewis, N. S.; Schaak, R. E. Electrocatalytic and Photocatalytic Hydrogen Production from Acidic and Neutral-pH Aqueous Solutions Using Iron Phosphide Nanoparticles. *ACS Nano* **2014**, *8*, 11101−11107.

(17) Sun, M.; Liu, H.; Qu, J.; Li, J. Earth-Rich Transition Metal Phosphide for Energy Conversion and Storage. *Adv. Energy Mater.* **2016**, *6*, No. 1600087.

(18) He, P.; Yu, X.; Lou, X. W. (David). Carbon-Incorporated Nickel−Cobalt Mixed Metal Phosphide Nanoboxes with Enhanced Electrocatalytic Activity for Oxygen Evolution. *Angew. Chem., Int. Ed.* **2017**, *56*, 3897−3900.

(19) Trotochaud, L.; Young, S. L.; Ranney, J. K.; Boettcher, S. W. Nickel−Iron Oxyhydroxide Oxygen-Evolution Electrocatalysts: The Role of Intentional and Incidental Iron Incorporation. *J. Am. Chem. Soc.* **2014**, *136*, 6744−6753.

(20) Tahir, M.; Pan, L.; Idrees, F.; Zhang, X.; Wang, L.; Zou, J.-J.; Wang, Z. L. Electrocatalytic Oxygen Evolution Reaction for Energy Conversion and Storage: A Comprehensive Review. *Nano Energy* **2017**, *37*, 136−157.

(21) Cai, Z.; Zhou, D.; Wang, M.; Bak, S.; Wu, Y.; Wu, Z.; Tian, Y.; Xiong, X.; Li, Y.; Liu, W.; Siahrostami, S.; Kuang, Y.; Yang, X.; Duan, H.; Feng, Z.; Wang, H.; Sun, X. Introducing Fe^{2+} into Nickel−Iron Layered Double Hydroxide: Local Structure Modulated Water Oxidation Activity. *Angew. Chem., Int. Ed.* **2018**, *57*, 9392−9396.

(22) Yu, L.; Wu, L.; McElhenny, B.; Song, S.; Luo, D.; Zhang, F.; Yu, Y.; Chen, S.; Ren, Z. Ultrafast Room-Temperature Synthesis of Porous S-Doped Ni/Fe (Oxy)Hydroxide Electrodes for Oxygen Evolution Catalysis in Seawater Splitting. *Energy Environ. Sci.* **2020**, *13*, 3439−3446.

(23) Li, Y.; Gong, M.; Liang, Y.; Feng, J.; Kim, J.-E.; Wang, H.; Hong, G.; Zhang, B.; Dai, H. Advanced Zinc-Air Batteries Based on High-Performance Hybrid Electrocatalysts. *Nat. Commun.* **2013**, *4*, 1805.

(24) Chen, F.; Guo, S.; Yu, S.; Zhang, C.; Guo, M.; Li, C. Hierarchical N-Doped Carbon Nanofiber-Loaded NiCo Alloy Nanocrystals with Enhanced Methanol Electrooxidation for Alkaline Direct Methanol Fuel Cells. *J. Colloid Interface Sci.* **2023**, *646*, 43−53.

(25) Gao, K.; Wang, B.; Tao, L.; Cunning, B. V.; Zhang, Z.; Wang, S.; Ruoff, R. S.; Qu, L. Efficient Metal-Free Electrocatalysts from N-Doped Carbon Nanomaterials: Mono-Doping and Co-Doping. *Adv. Mater.* **2019**, *31*, No. 1805121.

(26) Gautam, R. P.; Pan, H.; Chalyavi, F.; Tucker, M. J.; Barile, C. J. Nanostructured Ni−Cu Electrocatalysts for the Oxygen Evolution Reaction. *Catal. Sci. Technol.* **2020**, *10*, 4960−4967.

(27) Ding, S.; He, L.; Fang, L.; Zhu, Y.; Li, T.; Lyu, Z.; Du, D.; Lin, Y.; Li, J. Carbon-Nanotube-Bridging Strategy for Integrating Single Fe Atoms and NiCo Nanoparticles in a Bifunctional Oxygen Electrocatalyst toward High-Efficiency and Long-Life Rechargeable Zinc−Air Batteries. *Adv. Energy Mater.* **2022**, *12*, No. 2202984.

(28) Ramadhan, Z. R.; Poerwoprajitno, A. R.; Cheong, S.; Webster, R. F.; Kumar, P. V.; Cychy, S.; Gloag, L.; Benedetti, T. M.; Marjo, C. E.; Muhler, M.; Wang, D.-W.; Gooding, J. J.; Schuhmann, W.; Tilley, R. D. Introducing Stacking Faults into Three-Dimensional Branched Nickel Nanoparticles for Improved Catalytic Activity. *J. Am. Chem. Soc.* **2022**, *144*, 11094−11098.

(29) Lyu, Z.; Yu, S.; Wang, M.; Tieu, P.; Zhou, J.; Shi, Q.; Du, D.; Feng, Z.; Pan, X.; Lin, H.; Ding, S.; Zhang, Q.; Lin, Y. NiFe Nanoparticle Nest Supported on Graphene as Electrocatalyst for Highly Efficient Oxygen Evolution Reaction. *Small* **2024**, *20*, 2308278.

(30) Lu, X.; Zhao, C. Electrodeposition of Hierarchically Structured Three-Dimensional Nickel−Iron Electrodes for Efficient Oxygen Evolution at High Current Densities. *Nat. Commun.* **2015**, *6*, 6616.

(31) Jia, Y.; Zhang, L.; Gao, G.; Chen, H.; Wang, B.; Zhou, J.; Soo, M. T.; Hong, M.; Yan, X.; Qian, G.; Zou, J.; Du, A.; Yao, X. A Heterostructure Coupling of Exfoliated Ni−Fe Hydroxide Nanosheet and Defective Graphene as a Bifunctional Electrocatalyst for Overall Water Splitting. *Adv. Mater.* **2017**, *29*, No. 1700017.

(32) Lu, B.; Liu, Q.; Wang, C.; Masood, Z.; Morris, D. J.; Nichols, F.; Mercado, R.; Zhang, P.; Ge, Q.; Xin, H. L.; Chen, S. Ultrafast Preparation of Non-Equilibrium Fe-Ni Spinels by Magnetic Induction Heating for Unprecedented Oxygen Evolution Electrocatalysis. *Research* **2022**, *2022*, No. 9756983.

(33) Cheng, H.; Yang, N.; Lu, Q.; Zhang, Z.; Zhang, H. Syntheses and Properties of Metal Nanomaterials with Novel Crystal Phases. *Adv. Mater.* **2018**, *30*, No. 1707189.

(34) Wu, Z.-P.; Shan, S.; Xie, Z.-H.; Kang, N.; Park, K.; Hopkins, E.; Yan, S.; Sharma, A.; Luo, J.; Wang, J.; Petkov, V.; Wang, L.; Zhong, C.-J. Revealing the Role of Phase Structures of Bimetallic Nanocatalysts in the Oxygen Reduction Reaction. *ACS Catal.* **2018**, *8*, 11302−11313.

(35) Wang, C.; Yang, H.; Zhang, Y.; Wang, Q. NiFe Alloy Nanoparticles with HCP Crystal Structure Stimulate Superior Oxygen Evolution Reaction Electrocatalytic Activity. *Angew. Chem., Int. Ed.* **2019**, *58*, 6099−6103.

(36) Zheng, X.; Zhang, B.; De Luna, P.; Liang, Y.; Comin, R.; Voznyy, O.; Han, L.; García De Arquer, F. P.; Liu, M.; Dinh, C. T.; Regier, T.; Dynes, J. J.; He, S.; Xin, H. L.; Peng, H.; Prendergast, D.; Du, X.; Sargent, E. H. Theory-Driven Design of High-Valence Metal Sites for Water Oxidation Confirmed Using in Situ Soft X-Ray Absorption. *Nat. Chem.* **2018**, *10*, 149−154.

(37) Liang, C.; Zou, P.; Nairan, A.; Zhang, Y.; Liu, J.; Liu, K.; Hu, S.; Kang, F.; Fan, H. J.; Yang, C. Exceptional Performance of Hierarchical Ni−Fe oxyhydroxide@NiFe Alloy Nanowire Array Electrocatalysts for Large Current Density Water Splitting. *Energy Environ. Sci.* **2020**, *13*, 86−95.

(38) Han, Q.; Luo, Y.; Li, J.; Du, X.; Sun, S.; Wang, Y.; Liu, G.; Chen, Z. Efficient NiFe-Based Oxygen Evolution Electrocatalysts and Origin of Their Distinct Activity. *Appl. Catal. B: Environ.* **2022**, *304*, No. 120937.

(39) Zhang, J.; Zhang, L.; Du, L.; Xin, H. L.; Goodenough, J. B.; Cui, Z. Composition-Tunable Antiperovskite $Cu_xIn_{1-x}NNi_3$ as

Superior Electrocatalysts for the Hydrogen Evolution Reaction. *Angew. Chem., Int. Ed.* **2020**, *59*, 17488−17493.

(40) Friebel, D.; Louie, M. W.; Bajdich, M.; Sanwald, K. E.; Cai, Y.; Wise, A. M.; Cheng, M.-J.; Sokaras, D.; Weng, T.-C.; Alonso-Mori, R.; Davis, R. C.; Bargar, J. R.; Nørskov, J. K.; Nilsson, A.; Bell, A. T. Identification of Highly Active Fe Sites in (Ni,Fe)OOH for Electrocatalytic Water Splitting. *J. Am. Chem. Soc.* **2015**, *137*, 1305−1313.

(41) Yao, Y.; Huang, Z.; Xie, P.; Lacey, S. D.; Jacob, R. J.; Xie, H.; Chen, F.; Nie, A.; Pu, T.; Rehwoldt, M.; Yu, D.; Zachariah, M. R.; Wang, C.; Shahbazian-Yassar, R.; Li, J.; Hu, L. Carbothermal Shock Synthesis of High-Entropy-Alloy Nanoparticles. *Science* **2018**, *359*, 1489−1494.

(42) Liu, X.; Wan, X.; Tan, X.; Yang, H.; Yang, Y.; Shui, J.; Wang, X. Nanoscale Pt_5Ni_{36} Design and Synthesis for Efficient Oxygen Reduction Reaction in Proton Exchange Membrane Fuel Cells. *J. Mater. Chem. A* **2021**, *9*, 21051−21056.

(43) Zheng, J.; Zhang, J.; Zhang, L.; Zhang, W.; Wang, X.; Cui, Z.; Song, H.; Liang, Z.; Du, L. Ultrafast Carbothermal Shock Constructing $Ni_3Fe_{1-x}Cr_x$ Intermetallic Integrated Electrodes for Efficient and Durable Overall Water Splitting. *ACS Appl. Mater. Interfaces* **2022**, *14*, 19524−19533.

(44) Sun, J.; Zhao, Z.; Li, Z.; Zhang, Z.; Zhang, R.; Meng, X. Ultrafast Carbothermal Shocking Fabrication of Cation Vacancy-Rich Mo Doped Ru Nanoparticles on Carbon Nanotubes for High-Performance Water/Seawater Electrolysis. *J. Mater. Chem. A* **2023**, *11*, 22430−22440.

(45) Fan, Z.; Guo, X.; Yang, M.; Jin, Z. Mechanochemical Preparation and Application of Graphdiyne Coupled with CdSe Nanoparticles for Efficient Photocatalytic Hydrogen Production. *Chin. J. Catal.* **2022**, *43*, 2708−2719.

(46) Lu, Y.; Chen, Y.; Li, Q.; Hao, Z.; Wang, L.; Qiu, D.; He, C.; Wang, M.; Cui, X. Regulating Symmetry of Organic Precursors for Mechanochemical Synthesizing Rich Pyridonic-/Pyridinic-Nitrogen Doped Graphyne. *Carbon* **2022**, *194*, 274−281.

(47) Smith, W. F.; Hashemi, J. *Foundations of Materials Science and Engineering.*; McGraw-Hill Companies, Inc., 2010.

(48) Wang, D.; Le, F.; Lv, J.; Yang, X.; Chen, X.; Yao, H.; Jia, W. Fe-Incorporated Nickel-Based Bimetallic Metal−Organic Frameworks for Enhanced Electrochemical Oxygen Evolution. *Molecules* **2023**, *28*, 4366.

(49) Yang, X.; Zhao, F.; Yeh, Y.-W.; Selinsky, R. S.; Chen, Z.; Yao, N.; Tully, C. G.; Ju, Y.; Koel, B. E. Nitrogen-Plasma Treated Hafnium Oxyhydroxide as an Efficient Acid-Stable Electrocatalyst for Hydrogen Evolution and Oxidation Reactions. *Nat. Commun.* **2019**, *10*, 1543.

(50) Zhao, B.; Liu, J.; Xu, C.; Feng, R.; Sui, P.; Wang, L.; Zhang, J.; Luo, J.; Fu, X. Hollow NiSe Nanocrystals Heterogenized with Carbon Nanotubes for Efficient Electrocatalytic Methanol Upgrading to Boost Hydrogen Co-Production. *Adv. Funct. Mater.* **2021**, *31*, No. 2008812.

(51) Louie, M. W.; Bell, A. T. An Investigation of Thin-Film Ni−Fe Oxide Catalysts for the Electrochemical Evolution of Oxygen. *J. Am. Chem. Soc.* **2013**, *135*, 12329−12337.

(52) Yang, N.; Tian, S.; Feng, Y.; Hu, Z.; Liu, H.; Tian, X.; Xu, L.; Hu, C.; Yang, J. Introducing High-Valence Iridium Single Atoms into Bimetal Phosphides toward High-Efficiency Oxygen Evolution and Overall Water Splitting. *Small* **2023**, *19*, No. 2207253.

(53) Bai, Y.; Wu, Y.; Zhou, X.; Ye, Y.; Nie, K.; Wang, J.; Xie, M.; Zhang, Z.; Liu, Z.; Cheng, T.; Gao, C. Promoting Nickel Oxidation State Transitions in Single-Layer NiFeB Hydroxide Nanosheets for Efficient Oxygen Evolution. *Nat. Commun.* **2022**, *13*, 6094.

(54) Zheng, Q.; Yan, Y.; Zhong, J.; Yan, S.; Zou, Z. Reagent-Adaptive Active Site Switching on the $IrO_x/Ni(OH)_2$ Catalyst. *Energy Environ. Sci.* **2024**, *17*, 748−759.

(55) Park, J. E.; Kang, S. Y.; Oh, S.-H.; Kim, J. K.; Lim, M. S.; Ahn, C.-Y.; Cho, Y.-H.; Sung, Y.-E. High-Performance Anion-Exchange Membrane Water Electrolysis. *Electrochim. Acta* **2019**, *295*, 99−106.